PNAS
www.pnas.org

Supplementary Information for

Neuronal ROS-induced glial lipid droplet formation is altered by loss of Alzheimer's disease-associated genes

Matthew J. Moulton, Scott Barish, Isha Ralhan, Jinlan Chang, Lindsey D. Goodman, Jake G. Harland, Paul C. Marcogliese, Jan O. Johansson, Maria S. Ioannou, and Hugo J. Bellen

Corresponding author: Hugo J. Bellen
Email: hbellen@bcm.edu

This PDF file includes:

Supplementary Information

Drosophila photoreceptor neurons and pigment glia lie in close proximity in the retina allowing the interactions between these cells to be readily probed. (Supp. Fig. 1A). Neuronal ROS induces glial LD formation and this process requires the apolipoprotein, Glial Lazarillo (GLaz; homolog to human APOD; Supp. Fig. 1B). We have previously reported that pigment glia transport lactate to neurons, through monocarboxylate transporters, which is converted to pyruvate and Acetyl-CoA in order to support the TCA cycle in mitochondria (1, 2). However, defective mitochondria do not optimally utilize this energy source and simultaneously produce ROS, which activates JNK and SREBP transcription factors that drive lipid synthesis using newly formed Acetyl-CoA from the mitochondria (Supp. Fig. 1B). These lipids become peroxidated in the presence of ROS and are subsequently transported intracellularly via fatty acid transport proteins (FatP) to a heretofore unknown lipid exporter. While ROS induction causes the eventual demise of photoreceptor neurons, activation of neuronal lipogenesis via photoreceptor-specific overexpression of JNK or SREBP, in the absence of ROS, induces LD formation but does not affect neuronal viability or function (1). Hence, lipid peroxidation, but not lipid production alone, causes photoreceptor neurotoxicity.

Using the fly as a model, we set out to identify genes that are critical for glial LD formation upon neuronal ROS activation. We recognized the enrichment of AD risk-associated genes in lipid handling and endocytosis in GWAS and hypothesized that these genes may be involved in glial LD formation. We tested this hypothesis by targeting candidate orthologs of AD risk genes via RNAi using tissue-specific expression drivers (Supp. Figure 1C). LD formation does not occur in the absence of neuronal ROS, even in the presence of RNAi targeting the genes of interest (Supp. Fig. 2). This suggests that the

LD attenuation phenotypes observed are specific to the knockdown of target genes in the presence of neuronal ROS. RNAi expression was highly effective at eliminating at least 50% of detectable transcripts of the target genes in this study (Supp. Fig. 3), thus providing an effective platform in which to examine the role of candidate genes in glial LD formation.

In an effort to identify the role of AD-risk genes ABCA1 and ABCA7 in our fly model of neuronal ROS-induced glial LD formation, it was necessary to identify the fly orthologs of these genes. The fly genome contains 10 putative ABCA transporters compared to 13 ABCA transporters in humans, and pairwise analysis of protein sequence does not reveal an obvious 1:1 orthology. To identify fly ABCA proteins that share the greatest homology with ABCA1 and ABCA7 we assembled a gene tree of human and fly ABCA protein sequences. We found that fly genes *ldd* and *Eato* grouped most closely with human ABCA1/2/4/7/12/13 suggesting that these two fly genes may be orthologs of this monophyletic group of human transporters that includes ABCA1 and ABCA7 (Supp. Fig. 4A). Homology between *ABCA1*/*7* and *Eato*/*ldd* is further supported by *in silico* ortholog prediction tools including DIOPT (Supp. Fig. 4B). Further studies aimed at delineating receptor function and specificity are warranted and will likely aid the delineation of orthologous relationships within the complex ABCA family.

Targeted knockdown of the ABCA genes *Eato* and *ldd* in fly neurons reduced glial LD formation and loss of glial LD formation is associated with neuronal demise (1, 2). We set out to test whether neurodegeneration occurred in conditions of glial LD loss. Neurodegeneration was first assessed by staining retinas with Nile Red to observe photoreceptor rhabdomeres. Misshapen or missing rhabdomeres is indicative of the onset

of neurodegeneration (3) and was observed in the retinas of animals in which neuronal ROS and knockdown of key LD formation genes occurred (Supp. Fig. 5A-C).

We also examined the role for endocytic genes in glial LD formation and neurodegeneration including *BIN1*, *CD2AP*, *PICALM*, *AP2A2*, and *RIN3*, which have all been implicated as AD risk factors. We found no difference in LD formation phenotypes when *RIN3* (*spri*) and *BIN1* (*amph*) were targeted by RNAi in either neurons or glia (Supp. Fig. 6) suggesting that neither of these genes is required for glial LD formation. As before, we assessed neurodegeneration in these lines by evaluating photoreceptor rhabdomere morphology and loss. Under conditions where LD formation was lost, we observed misshapen or missing rhabdomeres, indicative of neurodegeneration initiation (Supp. Fig. 5D-H). Together, these data indicate that ABCA and endocytic genes are critical for glial LD formation and the prevention of neuronal loss upon ROS activation.

ROS activation also has the capacity to exacerbate neuronal demise and amyloid-induced phenotypes which was established in the fly model and in a mouse model of Aβ42 expression (see Fig. 5). ROS levels in mouse brains was quantified using Western blot analysis and we confirmed that elevated ROS occurs in the brains of mice reared in hyperoxia, regardless of genotype (Supp. Fig. 7A). Aβ42 plaque number and size was quantified in several brain regions including in the hindbrain (Supp. Fig. 7B-C). In this region, plaque size and number was elevated in 5XFAD mice compared to wild-type control mice regardless of their oxygen exposure. To ensure adequate statistical power of the mouse study of amyloid plaques in the brain, a post-hoc power analysis was performed in G*Power 3.1 (4) using a calculated Cohen's d effect size for each analysis and α error

probability of 0.05. Power analysis revealed that this study is properly powered (Power>0.9 for all comparisons that yielded statistically significant changes) (Supp. Table 2).

Together, our data implicate a close interaction between ROS, LD formation, and genes implicated as AD risk factors. We have previously demonstrated that in the presence of neuronal ROS, human APOE4 is incapable of inducing glial LD formation and leads to neuronal demise and dysfunction as seen in Nile Red staining and in ERG studies (Supp. Fig. 8A, C, E). These defects can be rescued by the expression of an ABCA1 agonist peptide (CS6253) in the humanized APOE4 fly model (Supp. Fig. 8B, D, F) suggesting that restoration of the LD pathway can prevent ROS-induced neurodegeneration.

Supplementary Materials and Methods

Drosophila husbandry and transgenesis: Stock genotypes and availability is listed in Supplemental Table 1. For consistency with previous studies, we utilized female flies, though LD phenotypes can be observed in both sexes. For transgenic animals, ORF synthesis was designed in pUC57 using Drosophila codon-optimized sequence (Integrated DNA Technologies) of the argos secretion signal (MPTTLMLLPCMLLLLLTAAAVAVGG) (3) upstream of the peptide sequence, where citrulline residues were replaced with arginine residues, (EVRSKLEEWLAALRELAEELLARAKS) (5, 6). The ORF was shuttled to the Gateway pDONR221 entry vector (ThermoFisher) by BP clonase II reaction (ThermoFisher) using Argos_attB primers. Fully sequence verified clones were shuttled to the pGW-attB-HA destination vector (7) by LR clonase II (ThermoFisher). The UAS construct was inserted into the VK37 (PBac{y[+]-attP}VK00037) docking site by ϕC31 mediated transgenesis (8).

Mouse husbandry: Mice were housed under 12-hour light/dark conditions at 22°C with standard chow diet (5053; Picolab) and water available ad libitum. Stock genotypes and availability is listed in Supp. Table 1. Hyperoxia experiments were performed using the A-Chamber animal cage enclosure (BioSpherix) with oxygen levels regulated using the ProOx360 High Infusion Rate O2 Controller (BioSpherix).

Rotenone Feeding: A stock solution of 10mM Rotenone was made in DMSO and diluted to 25µM in liquid fly food. Bromophenol blue was added to the solution to monitor food intake by the flies. Adult flies were placed into rotenone, or DMSO-alone vials for comparison, and stored in dark conditions to prevent breakdown of the rotenone in the food. Rotenone food was changed every 3-5 days to retain drug potency.

LD Analysis: Fly heads were isolated under PBS and fixed in 3.7% formaldehyde overnight. Retinas were then dissected under PBS and rinsed three times with 1X PBS and incubated for 20 minutes at 1:1,000 dilution of PBS with 1 mg/mL Nile Red (Millipore Sigma). Retinas were subsequently rinsed five times with 1X PBS and mounted in Vectashield (Vector Labs) for imaging on a Leica SP8 confocal microscope. Images were obtained using a 63x glycerol submersion lens with 3x zoom.

Toluidine blue staining of whole-mount fly retinas: Fly heads were isolated under modified Karnovksy's fixative (2.5% glutaraldehyde, 2% paraformaldehyde in 0.1 M cacodylate buffer) and embedded in paraffin. Retinal sections were prepared on using the Leica UC7 Ultramicrotome, stained with toluidine blue, and imaged using the JEOL JEM 1010 microscope using a 20x objective.

ERG analysis: Live flies were immobilized with Elmer's school glue on a microscope slide. Glass electrodes, filled with 100 mM NaCl, were placed in the thorax for reference and on the center part of the eye for recording. Prior to recording, flies were maintained in the dark for at least one minute. Approximately one-second light flashes were manually delivered using a halogen lamp. At least three recordings from at least 10 flies per genotype were obtained for analysis using the LabChart 8 (AD Instruments) data pad tool. Data sets were exported to Microsoft Excel for statistical analysis.

Gene Tree Assembly: Protein sequences of all human and fly ABCA genes were downloaded from the National Center for Biotechnology Information (NCBI) website. Sequences were aligned using ClustalW algorithm within MEGA X (9) using default parameters. Aligned sequences were then used to build a neighbor-joining tree using MEGA X.

qRT-PCR Analysis: Ten larvae ubiquitously expressing RNAi, via *da-GAL4*, were isolated. RNA extraction was carried out using the RNeasy Mini Kit (Qiagen) followed by reverse transcription into cDNA using iScript Reverse Transcription Supermix (BioRad). Quantitative PCR reactions were performed using iTaq Universal SYBR Green Supermix (BioRad) on a BioRad CFX96 Touch Real-Time PCR Detection System. Three biological and technical replicates were performed for each genotype. Expression (Ct) values were obtained and used to calculate differential expression (ΔCt) and normalized to GAPDH expression.

Immunohistochemistry: Mice were anesthetized with and sacrificed by intracardiac perfusion, initially with saline, followed by 4% paraformaldehyde in PBS. Mouse brains were removed and bisected down the midline with one hemibrain utilized for histopathological analysis, which was immersed again in paraformaldehyde for 24 hours at 4°C. Hemibrains were then dehydrated and preserved in paraffin. Serial sagittal sections were cut and 6 µM sections were mounted on glass slides. After sections were blocked in 10% normal goat serum and rinsed with PBS, sections were stained with the anti-Aβ42 antibody (Covance, 1:1,000) and a biotinylated anti-mouse IgG antibody (Jackson, 1:200). Slides were then incubated in DAB solution, monitored by eye, and the reaction stopped with distilled water. Finally, slides were counterstained using Mayer's hematoxylin and dehydrated prior to imaging.

Primary culture of hippocampal neurons and astrocytes: Tissue was digested with papain, gently triturated, and filtered with a cell strainer and plated on poly-D-lysine coated coverslips for the transfer assay or plastic tissue culture dishes for Western blot analysis. Neurons were grown in Neurobasal medium containing B-27 supplement, 2 mM Glutamax

and antibiotic-antimycotic. Astrocytes were grown in Basal Eagle Media containing 10% fetal bovine serum, 0.45% glycose, 1 mM sodium pyruvate, 2 mM Glutamax, and antibiotic-antimycotic. All cells were grown at 37ºC in 5% CO_2.

Lentivirus transduction: Astrocytes at DIV 2 were transduced with SMARTVector lentiviral shRNA (Dharmacon) at an MOI of 3. Three independent shRNA sequences targeting PICALM or a non-targeting control shRNA was used. The media was replaced with fresh culture media after 24 hrs and the cells were used for protein validation or in the transfer assay 5 days later (DIV 7). To validate protein knockdown, astrocytes were lysed in lysis buffer [20 mM HEPES pH 7.4, 100 mM NaCl, 1% Triton X-100, 5 mM EDTA, 1× Halt Protease & Phosphatase Inhibitor Cocktail (Thermo Scientific)], resolved by SDS–PAGE and processed for Western blotting using anti-PICALM rabbit polyclonal (Millipore Sigma) and anti-GAPDH mouse monoclonal (ThermoFisher) as a loading control. Lysates were run in duplicate and statistics were performed on the average of these duplicates for each experiment.

Fatty acid transfer assay: Neurons at DIV 7 were incubated with 2 μM BODIPY 558/568 (Red-C12) for 16 hours in neuronal growth media. Neurons were washed twice with warm phosphate-buffered saline (PBS) and incubated with fresh media for 1 hour. Red-C12 labelled neurons and unlabeled astrocytes transduced with lentivirus as described above were washed twice with warm PBS and the coverslips were cultured together (facing each other), separated by paraffin wax and incubated in Hank's Balanced Salt solution containing calcium and magnesium for 4 hours at 37°C (10, 11). Astrocytes were fixed in 4% paraformaldehyde, stained with DAPI, and mounted using DAKO fluorescence mounting media. Images were acquired using a Zeiss 710 Laser Scanning Confocal

Microscope equipped with a plan-apochromat 63x oil objective (Zeiss, NA = 1.4). Maximum intensity projections of three-dimensional image stacks (0.5µm sections) of Red-C12 staining were obtained and analyzed using ImageJ. Only astrocytes expressing the lentiviral reporter turboGFP were quantified. Images were thresholded and the number of particles with a pixel size greater than 2 was detected. 10 cells per coverslip were averaged. Schematic of fatty acid transfer assay was created with BioRender.com.

Fig. S1. Neuron-to-glia lipid transfer for lipid droplet formation.

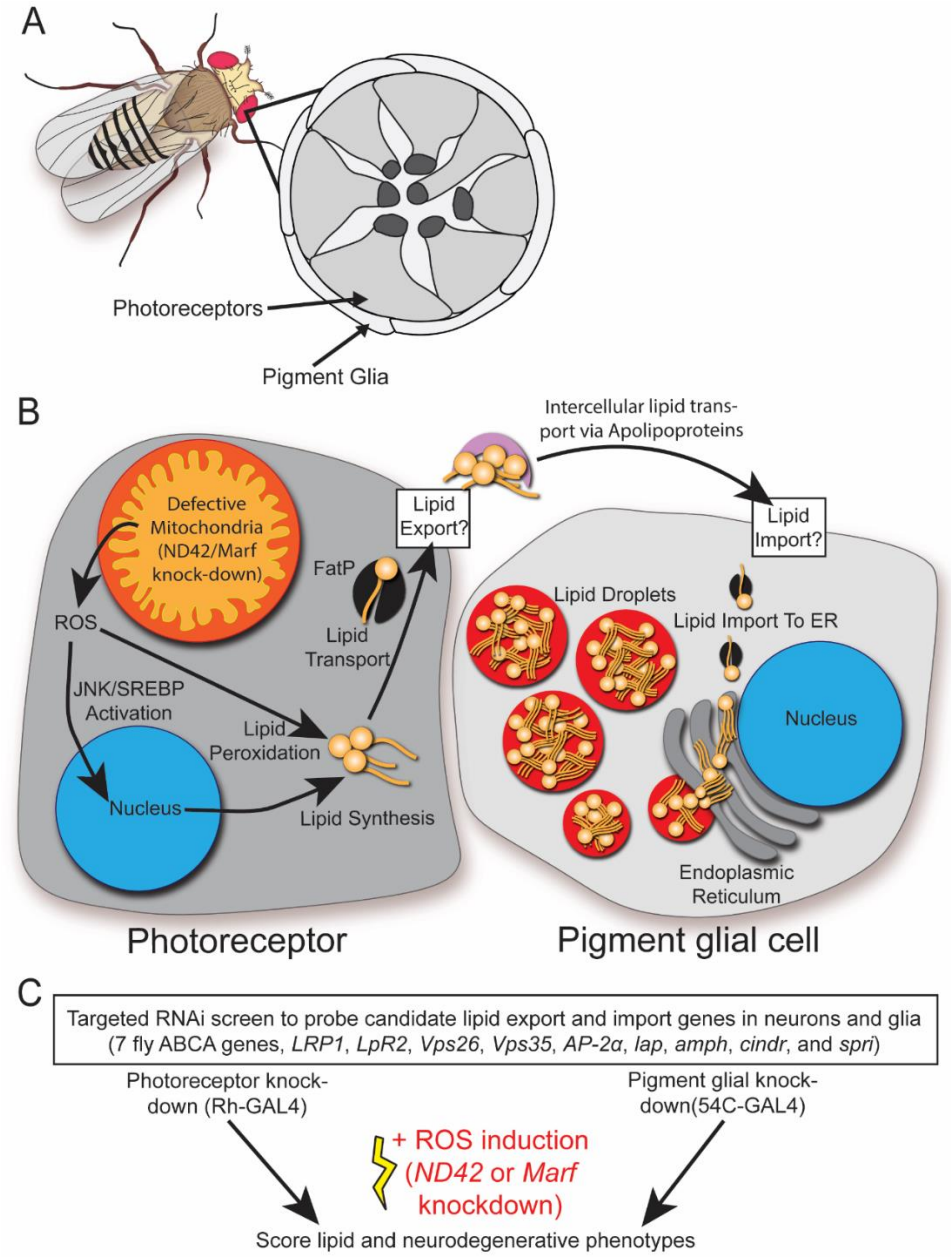

(A) The Drosophila eye was utilized in this study as a model of lipid transfer between neurons and glia. There are 7 visible photoreceptor neurons (with central rhabdomeres) in each optical section through a fly ommatidium, which are surrounded by pigment glia. (B) Neurons and glia in the Drosophila visual system have a tightly regulated method of lipid production, transfer, and lipid droplet (LD) formation. Defective mitochondria produce ROS which drives the synthesis of lipids. Lipids are transported intracellularly via FatP and extracellularly via apolipoproteins where they are taken up in surrounding glia and incorporated into LDs (2). (C) Overview of targeted RNAi screen to identify genes critical for LD glial formation. Fly orthologs of human genes selected from candidate AD risk loci were targeted for RNAi knockdown in photoreceptors or pigment glia. ROS production was induced using previously characterized models of knockdown of *ND42* or *Marf* and lipid droplet formation and neurodegeneration phenotypes were scored.

Fig. S2. LD formation does not occur in the absence of neuronal ROS.

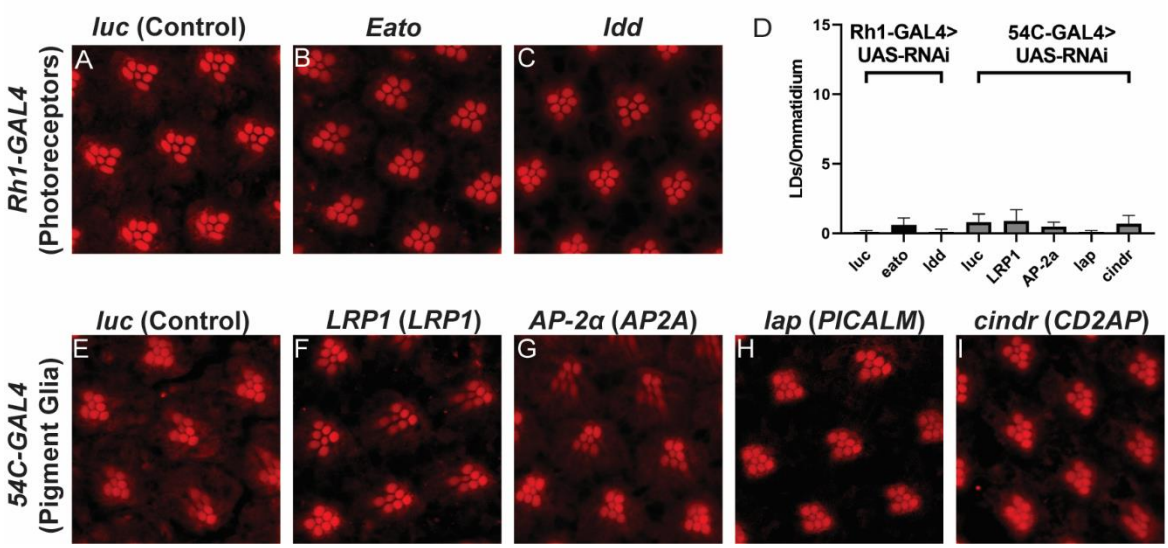

LD analysis in animals reared for 24 hrs post eclosion at 29°C under 12-hr light/dark conditions; representative images of ≥5 animals per genotype. LD formation does not occur in the absence of neuronal ROS upon photoreceptor-specific knockdown of control (luciferase), *Eato*, or *Idd* (A-C, black bars in D) or upon pigment glia-specific knockdown of control (luciferase), *LRP1*, *AP-2α*, *lap*, or *cindr* (E-I, grey bars in D). Mean ± SEM and one-way ANOVA analysis with post-hoc Tukey's test, *n* ≥5 for each genotype.

Fig. S3. Analysis of RNA expression of genes targeted in this study.

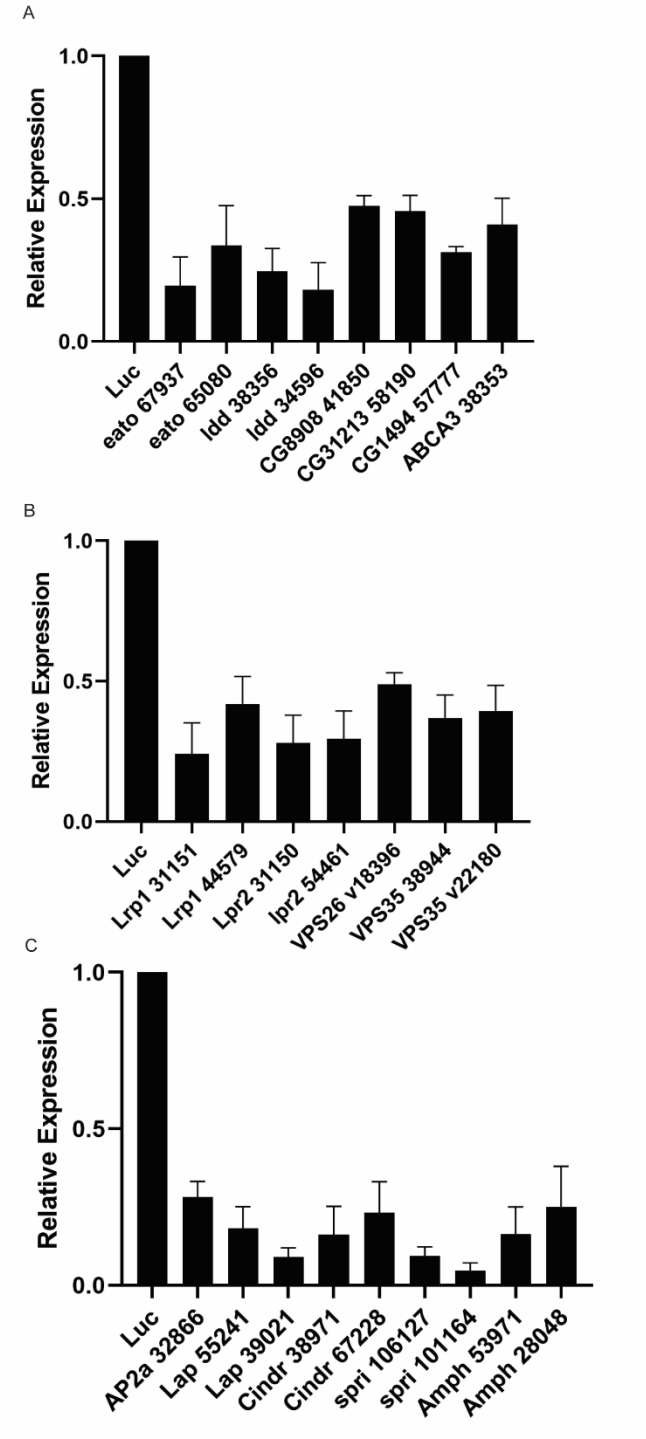

Quantification of mRNA expression of the genes assayed after ubiquitous (*da-GAL4*) RNAi induction by qRT-PCR in L3 larvae (A-C). Y-axis lists gene names followed by BDSC stock numbers. In each assay, a *luciferase* RNAi is used as a negative control. RNAi induces at least a 50% reduction of the detectible mRNA of all genes assayed. Mean ± SEM, *n* =5 animals from three independent runs.

Fig. S4. Fly and human ABCA protein tree and ortholog predictions.

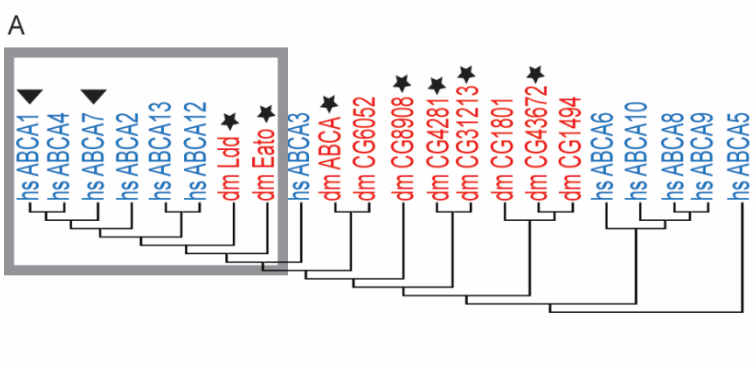

B

Human Gene	Fly Gene	DIOPT Score
ABCA1	Ldd	4
	ABCA	4
	CG6052	4
	CG8908	4
	Eato	4
ABCA7	Eato	4
	CG8908	4
	Ldd	4

(A) Protein tree of fly (red) and human (blue) ABCA transporter protein sequences. Human ABCA1 and ABCA7 have been implicated as AD risk genes (triangles). Stars indicate the fly genes that were assayed in this study. Grey square indicates monophyletic grouping of the fly proteins that group closest with AD risk proteins and paralogs. (B) *Eato* and *Ldd* are the closest homologs to the risk factors *ABCA1* and *ABCA7* based on phylogenetic analysis and prediction using the ortholog prediction tool DIOPT (12).

Fig. S5. Age-progressive degeneration of photoreceptors is evidenced by rhabdomere malformation and loss.

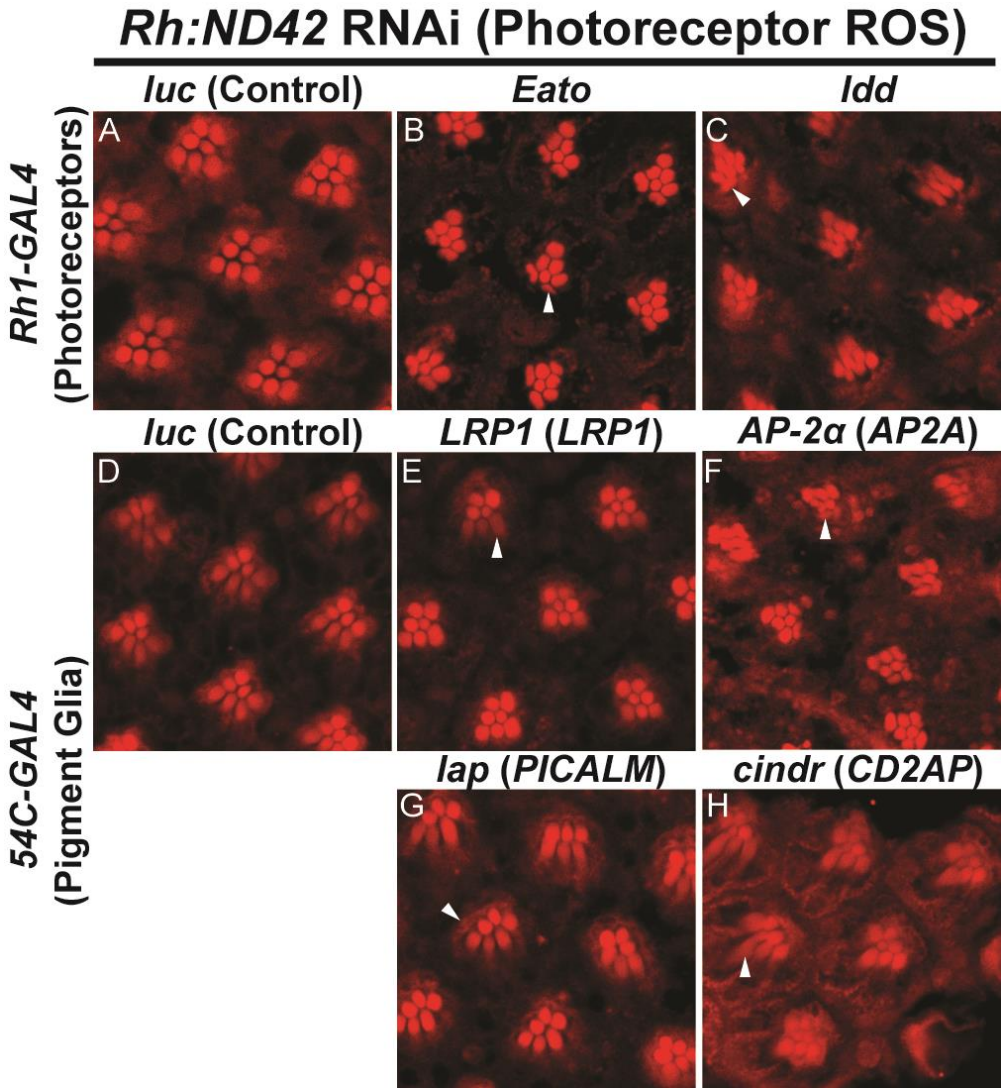

Nile Red staining of retinas from animals raised at 29° with 12-hr light/dark cycles for 20 d post eclosion. Photoreceptor rhabdomeres stain positively with Nile Red and 7 circular rhabdomeres are evident in each ommatidum in control animals. Misshapen rhabdomeres (indicative of dying photoreceptors) or missing rhabdomeres (indicative of dead photoreceptors) provide evidence of the onset of neurodegeneration. Neuronal ROS fails to induce evident neurodegeneration in control animals at d20 (A, D). The addition of neuronal RNAi targeting *Eato* and *Idd* (B-C) or glial RNAi targeting *LRP1*, *AP-2α*, *lap*, and *cindr* (E-H) leads to rhabdomere malformation or loss indicative of neurodegeneration.

Fig. S6. Loss of neuronal or glial Spri and Amph has non-significant effect on glial LD formation.

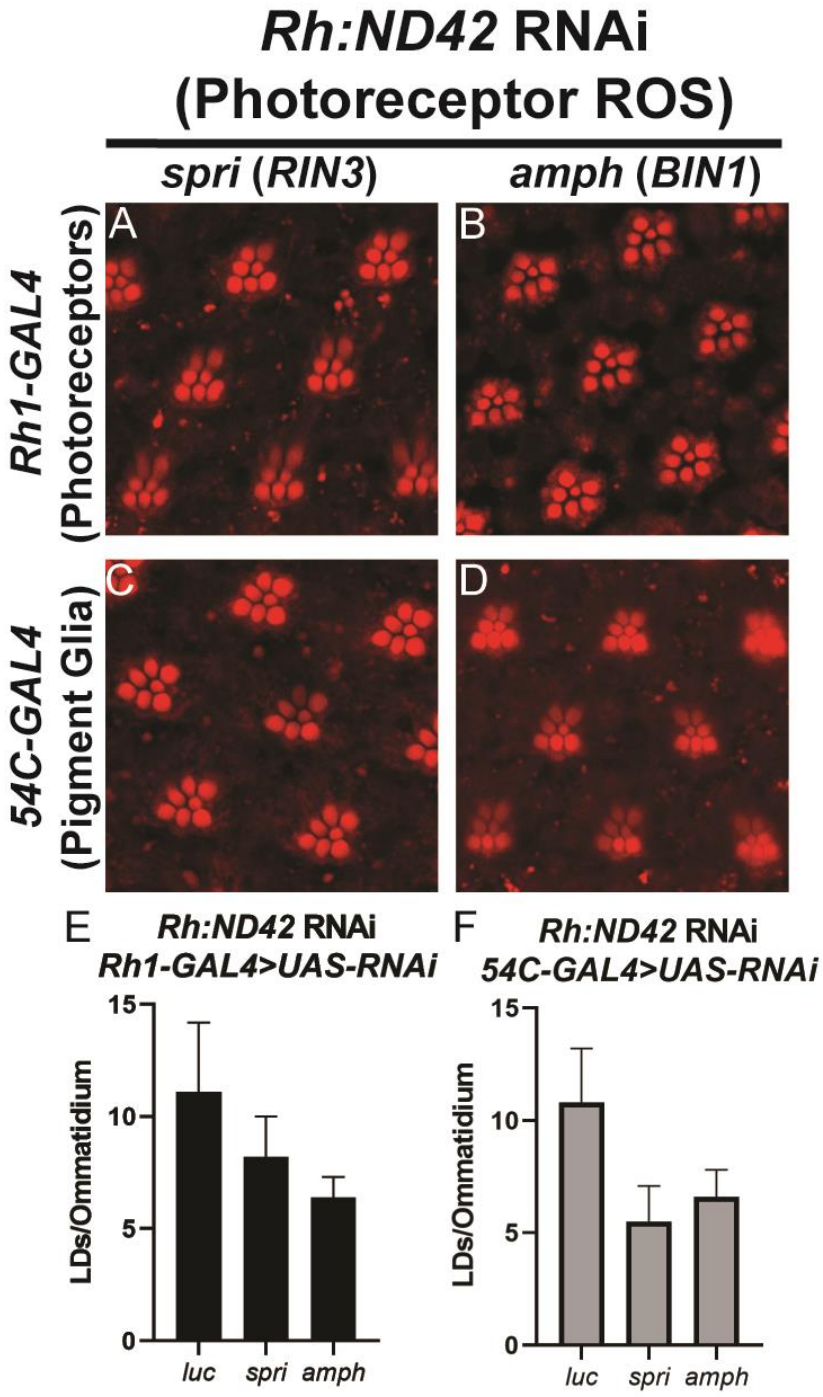

RNAi targeting spri and amph in neurons or glia did not statistically significantly alter LD formation (A-D) as quantified (E-F). Mean ± SEM and one-way ANOVA analysis with post-hoc Tukey's test, n≥10 for each genotype.

Fig. S7. Hyperoxia-induced ROS and hindbrain plaque quantification.

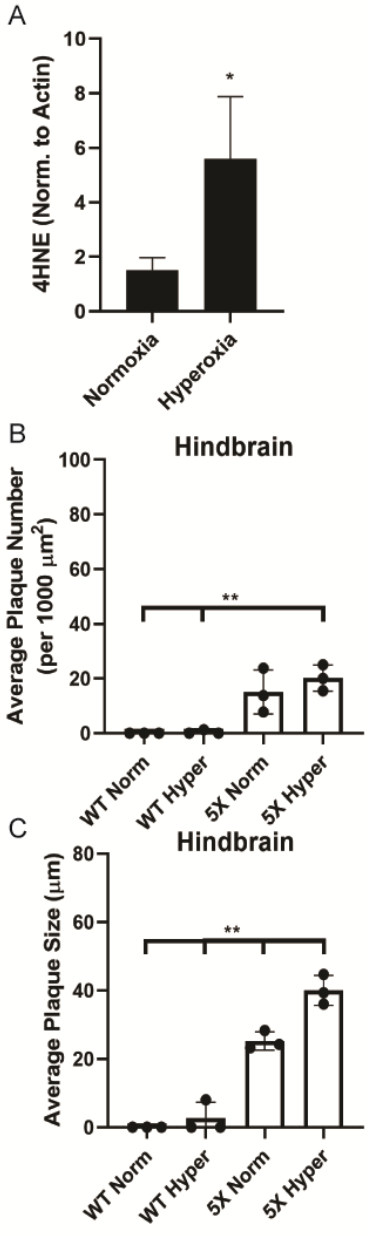

Brain ROS levels were quantified via Western blot analysis using an antibody directed against 4HNE (A). Band intensity from three blots was quantified using ImageJ, Mean +/- SEM plotted, pairwise t-Test, *p<0.05. Average Aβ42 plaque number (B) and size (C) from hindbrain of 5XFAD mice and littermate controls was quantified using ImageJ, Mean +/- SEM plotted, one-way ANOVA with post-hoc Tukey's test, **p<0.01.

Fig. S8. ABCA1 agonist peptide rescues rhabdomere loss and ERG phenotypes induced by ROS in an APOE4 background.

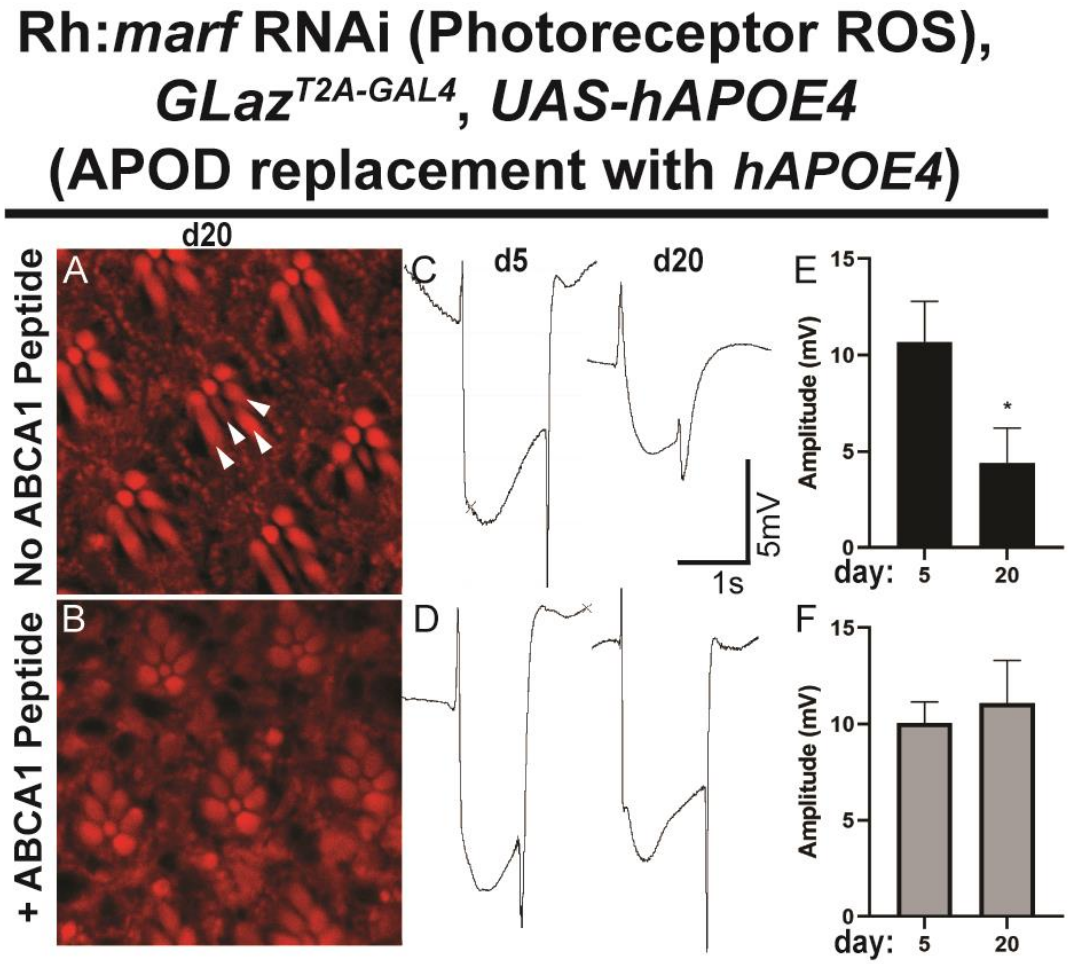

Neuronal ROS induction and expression of *APOE4* was induced as in Figure 6. Neurodegeneration onset is evident by 20 d post eclosion in the *APOE4* background (A) but is rescued, along with LD formation, in the presence of the ABCA1 agonist peptide (B). Age-dependent ERG amplitude deficits in the APOE4 background (C, E) are rescued with the expression of the ABCA1 agonist peptide (D, F).

Table S1. Normalized ROS levels as measured by Western blot analysis using an anti-4HNE antibody on protein lysates extracted from ND42 RNAi-expressing fly heads at 1 day post eclosion.

Gal4	UAS	ROS level (norm.)
Rh1	Empty	1.00
Rh1	VPS35 RNAi	0.38
Rh1	VPS26 RNAi	0.45
54C	Empty	1.00
54C	VPS35 RNAi	0.91
54C	VPS26 RNAi	0.88
54C	lap RNAi	1.62
54C	AP2-alpha RNAi	1.48

Table S2. Post hoc effect size and power calculations when comparing 5XFAD mice treated under hyperoxic and normoxic conditions.

	Effect Size (Cohen's *d*)	Power
Cortex plaque number	3.945347	0.9872191
Hindbrain plaque number	0.766705	0.1955491
Subiculum plaque number	2.993303	0.9087551
Cortex plaque size	4.595896	0.9977279
Hindbrain plaque size	4.060912	0.9903786
Subiculum plaque size	3.213697	0.9385959

Table S3. Resources utilized in this study

REAGENT	SOURCE	IDENTIFIER
Antibodies		
Anti Aβ42 (6E10)	Covance	RRID:AB_662798
Biotinylated anti-mouse IgG	Jackson Immuno. Res. Labs, Inc.	RRID:AB_2338557
Anti-4HNE	Abcam	RRID:AB_722490
Anti-PICALM rabbit polyclonal	Millipore Sigma	RRID:AB_1855361
Anti-GAPDH mouse monoclonal	ThermoFisher	RRID:AB_2536381
HRP- AffiniPure donkey anti-rabbit	Jackson Immuno. Res. Labs, Inc.	RRID:AB_2340770
HRP- AffiniPure donkey anti-mouse	Jackson Immuno. Res. Labs, Inc.	RRID:AB_2340770
Bacterial and Virus Strains		
SMARTvector hCMV-TurboGFP non-targeting control particles	Dharmacon Inc.	Cat# S-005000-01
SMARTvector Lentiviral Human PICALM hCMV-TurboGFP shRNA (shRNA1)	Dharmacon Inc.	Cat#V3SH7590-225194030
SMARTvector Lentiviral Human PICALM hCMV-TurboGFP shRNA (shRNA2)	Dharmacon Inc.	Cat#V3SH7590-225390149
SMARTvector Lentiviral Human PICALM hCMV-TurboGFP shRNA (shRNA3)	Dharmacon Inc.	Cat#V3SH7590-225119184
Chemicals, Peptides, and Recombinant Proteins		
Nile Red	Millipore Sigma	Cat # 72485
Rotenone	Millipore Sigma	Cat # R8875
N-acetylcysteine amide	Millipore Sigma	Cat # A0737
BODIPY 558/568 C12	ThermoFisher Sci.	Cat # D3835
Vectashield	Vector Labs	Cat # H-1000-10
4% paraformaldehyde	ThermoFisher Sci.	Cat # J61899-AK
BP clonase II	ThermoFisher Sci.	Cat # 11789020
LR clonase II	ThermoFisher Sci.	Cat # 11791020
RNeasy Mini Kit	Qiagen	Cat # 74104
iScript Rev. Transcription Supermix	BioRad	Cat # 1708840
iTaq Universal SYBR Green Supermix	BioRad	Cat # 1725120
DAPI	Abcam	Cat# ab228549
Halt protease & phosphatase inhibitor cocktail	ThermoFisher	Cat# 78446
DAKO fluorescence mounting media	Agilent Tech. Can. Inc.	Cat# S302380-2
Neurobasal medium	Gibco	Cat# LS21103049
Basal medium Eagle	Gibco	Cat# LS21010046
Fetal bovine serum	VWR Int'l. Ltd	Cat# MP97068-085
Sodium pyruvate	Gibco	Cat# LS11360070
Glutamax	Gibco	Cat# LS17504044
Antibiotic-antimycotic	Gibco	Cat# LS15240062
Poly-D-lysine	Millipore Sigma	Cat# P6407
Papain dissociation enzyme	Worthington Biochem.	Cat# LK003178
Hanks' Balanced Salt solution	Cytiva Life Sci.	Cat# SH3026801
Experimental Models: Organisms/Strains		
y1 w*; P{w[+m*] = GAL4}54C	D. melanogaster	BDSC_27328
P{NinaE-GD6220} (Rh-ND42 RNAi)	D. melanogaster	BDSC_76598

P{NinaE-GD11094} (Rh-Marf RNAi)	D. melanogaster	BDSC_76597
y1 w*; PBac{UAS-hAPOE.2.C112.C158} VK00037	D. melanogaster	BDSC_76604
y1 w*; PBac{UAS-APOE3.C112, R158} VK00037	D. melanogaster	BDSC_76605
y1 w*; PBac{UAS-APOE4.R112, R158} VK00037	D. melanogaster	BDSC_76607
y1 sc* v1 sev21; P{TRiP.HMS00653} attP2	D. melanogaster	BDSC_32866
y1 v1; P{TRiP.HMC02373}attP2	D. melanogaster	BDSC_55241
y1 v1; P{TRiP.HMS01939}attP40	D. melanogaster	BDSC_39021
y1 v1; P{TRiP.HMJ21356}attP40	D. melanogaster	BDSC_53971
y1 v1; P{TRiP.JF02883}attP2	D. melanogaster	BDSC_28048
y1 sc* v1 sev21; P{TRiP.HMS01795} attP2	D. melanogaster	BDSC_38328
y1 sc* v1 sev21; P{TRiP.HMS01892} attP40	D. melanogaster	BDSC_38976
y1 v1; P{TRiP.JF01627}attP2	D. melanogaster	BDSC_31150
y1 sc* v1 sev21; P{TRiP.HMS03722} attP2	D. melanogaster	BDSC_54461
y1 v1; P{TRiP.JF01628}attP2	D. melanogaster	BDSC_31151
y1 sc* v1 sev21; P{TRiP.HMS02875} attP2	D. melanogaster	BDSC_44579
P{KK105547}VIE-260B	D. melanogaster	VDRC_v106127,
P{KK102631}VIE-260B	D. melanogaster	VDRC_v101164,
y1 sc* v1 sev21; P{TRiP.HMS01858} attP40	D. melanogaster	BDSC_38944
w1118 P{GD11710}v22180	D. melanogaster	VDRC_v22180
w1118; P{GD8448}v18396	D. melanogaster	VDRC_v18396
y1 sc* v1 sev21; P{TRiP.GL01873} attP40	D. melanogaster	BDSC_67937
y1 sc* v1 sev21; P{TRiP.HMC06027} attP40	D. melanogaster	BDSC_65080
y1 v1; P{TRiP.HMS01824}attP40	D. melanogaster	BDSC_38356
y1 sc* v1 sev21; P{TRiP.HMS01070} attP2	D. melanogaster	BDSC_34596
y1 v1; P{TRiP.GL01278}attP2/TM3,Sb1	D. melanogaster	BDSC_41850
y1 sc* v1 sev21; P{TRiP.HMC04934} attP40	D. melanogaster	BDSC_58190
y1 sc* v1 sev21; P{TRiP.HMC04971} attP40	D. melanogaster	BDSC_57777
y1 v1; P{TRiP.HMS01821}attP40	D. melanogaster	BDSC_38353
y1 sc* v1 sev21; P{TRiP.HMC05641} attP40	D. melanogaster	BDSC_64606
SJL/J	M. musculus	RRID:IMSR_JAX:000686
B6SJL-Tg(APPSwFlLon,PSEN1*M146L* L286V)6799Vas/Mmjax	M. musculus	RRID:IMSR_JAX:033247
y1 w1118; PBac{y+-attP-3B}VK00037	D. melanogaster	BDSC_9752

Oligonucleotides

cindr_Exon3-4_F	CCTATGACTGGTAACCTTTTG
cindr_Exon4_R	GCTGCTCCAGATTCAGGTAGT
Ap-2a_Exon2-3_R	CCTCTTTGCTTTTGCAGTA
Ap-2a_Exon2_F	AGCTGAAGGGTGTGAAGTCG
lap_Exon8-9_F	TACGCAGTCATCAAGCTCGG
lap_Exon9_R	TCATAGCGGCTTCCTCTTCG

amph_Exon2-3_F	CATAAGATGTGTTCGCGCCG
amph_Exon3_R	CCACAGACTTTCCGAGGCAC
spri_Exon12-13_F	CCCTGGACTGGCGCTCCA
spri_Exon13_R	ACTTCACGGGTGGTGGTGT
lrp1_Exon5-6_R	GCTGGACAAGGACCTTTATCG
lrp1_Exon5_F	CAGCGGGCGCATCAATAGT
lpr2_Exon9-10_F	GTAGCAAGCGTCATCTATG
lpr2_Exon10_R	TGTGGCGTCCCATTCTTCTC
Argos_T6_attB1_F	GGGGACAAGTTTGTACAAAAAAGCAGGCTTCACCA TGCCCACCACTTTAATGCTGCTGC
Argos_T6_attB1_R	GGGGACCACTTTGTACAAGAAAGCTGGGTCCTAGC TCTTGGCGCGGGCCAGCAACTCC
CG34120_F	ATGGTCCTGGGTCTGATTGT
CG34120_R	AACACAGGCGAAGCTAAAGG
CG31731_F	TTCCTAGATCCCAAGACTTACATGA
CG31731_R	GTTCAAGTTGTCCGAAATTAGCG
ABCA_F	GTTATAGAGCTGGTGCTGCC
ABCA_R	GCAACGAATGTTGCAGCAGA
CG1494_F	AACAGGATCCACTGATGGGT
CG1494_R	AGATACCACTTGCCAGACGA
CG8908_F	AAGAAGTCGAGGACCAGTCG
CG8908_R	GTACTTCTCGCTGACAGTGC
CG31213_F	CGTGCAAACCTGAACGTACT
CG31213_R	CGGTTGGATAGCTTTGGCTT
CG42816_F	TCTGAAACCGAGTCATTGCG
CG42816_R	TTCCGTTTCATCCTCATGCTG
CG43672_F	TTACCCAAAGTCGTGATGCG
CG43672_R	TCCTCAACGATCAGCGTAGT
VPS26_Exon1-2_F	CGGTATCCGGCAAGGTGAAC
VPS26_Exon2_R	CGTGGTGGTTACCCCGGTCG
VPS35_Exon2-3_F	GCGAAGTGGCAAGACAAGTG
VPS35_Exon3_R	TGTCCATTCGGGTCTGCACG

Recombinant DNA

UAS-ArgosSS::Peptide		This study
pDONR221 entry vector	ThermoFisher	Cat # 12536017
pGW-attB-HA		Bischof et al., 2012

Software and Algorithms

FIJI	Schindelin, et al., 2012
Microsoft Excel 365	Microsoft Corp.
Adobe Illustrator 2020	Adobe
Adobe Photoshop 2020	Adobe
GraphPad Prism 8	GraphPad
LabChart 8	AD Instruments
Bio-Rad CFX Manager	Bio-Rad
GPower 3.1	UCLA

Other

A-Chamber Animal Cage Enclosure	BioSpherix	Cat # A66274P
ProOx 360 High Infusion Rate O2 Controller	BioSpherix	Cat # P360

SI References

1. L. Liu, *et al.*, Glial Lipid Droplets and ROS Induced by Mitochondrial Defects Promote Neurodegeneration. *Cell* **160**, 177–190 (2015).
2. L. Liu, K. R. MacKenzie, N. Putluri, M. Maletić-Savatić, H. J. Bellen, The Glia-Neuron Lactate Shuttle and Elevated ROS Promote Lipid Synthesis in Neurons and Lipid Droplet Accumulation in Glia via APOE/D. *Cell Metab.* **26**, 719-737.e6 (2017).
3. A. K. Chouhan, *et al.*, Uncoupling neuronal death and dysfunction in Drosophila models of neurodegenerative disease. *Acta Neuropathol. Commun.* **4**, 62–76 (2016).
4. E. Erdfelder, F. FAul, A. Buchner, A. G. Lang, Statistical power analyses using G*Power 3.1: Tests for correlation and regression analyses. *Behav. Res. Methods* **41**, 1149–1160 (2009).
5. J. K. Bielicki, ABCA1 agonist peptides for the treatment of disease. *Curr. Opin. Lipidol.* **27**, 40–46 (2016).
6. A. Boehm-Cagan, D. M. Michaelson, Reversal of apoE4-Driven Brain Pathology and Behavioral Deficits by Bexarotene. *J. Neurosci.* **34**, 7293–7301 (2014).
7. J. Bischof, *et al.*, A versatile platform for creating a comprehensive UAS-ORFeome library in Drosophila. *Dev.* **140**, 2434–2442 (2012).
8. K. J. T. Venken, Y. He, R. A. Hoskins, H. J. Bellen, P[acman]: A BAC transgenic platform for targeted insertion of large DNA fragments in D. melanogaster. *Science (80-.).* **314**, 1747–1751 (2006).
9. S. Kumar, G. Stecher, M. Li, C. Knyaz, K. Tamura, MEGA X: Molecular evolutionary genetics analysis across computing platforms. *Mol. Biol. Evol.* **35**, 1547–1549 (2018).
10. M. S. Ioannou, Z. Liu, J. Lippincott-Schwartz, A Neuron-Glia Co-culture System for Studying Intercellular Lipid Transport. *Curr. Protoc. Cell Biol.* **84**, 1–21 (2019).
11. M. S. Ioannou, *et al.*, Neuron-Astrocyte Metabolic Coupling Protects against Activity-Induced Fatty Acid Toxicity. *Cell* **177**, 1522-1535.e14 (2019).
12. Y. Hu, *et al.*, An integrative approach to ortholog prediction for disease-focused and other functional studies. *BMC Bioinformatics* **12** (2011).